Structural disorder of mechanically activated -mgcl2 studied by synchrotron x-ray total scattering and vibrational spectroscopy

catalysts

MDPI

Article

Structural Disorder of Mechanically Activated δ-$MgCl_2$ Studied by Synchrotron X-ray Total Scattering and Vibrational Spectroscopy

Toru Wada [1,2], Ashutosh Thakur [1], Patchanee Chammingkwan [1,2], Minoru Terano [1,2], Toshiaki Taniike [1,2,*], Alessandro Piovano [2,3] and Elena Groppo [2,3]

1 Graduate School of Advanced Science and Technology, Japan Advanced Institute of Science and Technology, 1-1 Asahidai, Nomi, Ishikawa 923-1292, Japan; toruwada@jaist.ac.jp (T.W.); thakur@jaist.ac.jp (A.T.); chamming@jaist.ac.jp (P.C.); terano@jaist.ac.jp (M.T.)
2 Dutch Polymer Institute (DPI), P.O. Box 902, 5600 AX Eindhoven, The Netherlands; alessandro.piovano@unito.it (A.P.); elena.groppo@unito.it (E.G.)
3 Department of Chemistry, INSTM and NIS Centre, University of Torino, Via Giuria 7, 10125 Torino, Italy
* Correspondence: taniike@jaist.ac.jp

Received: 28 August 2020; Accepted: 17 September 2020; Published: 20 September 2020

Abstract: A combination of synchrotron X-ray total scattering and molecular simulation is a powerful approach for reliable determination of the structure of δ-$MgCl_2$ as an indispensable component of heterogeneous Ziegler–Natta catalysts. Here, the same approach is applied to mechanically activated $MgCl_2$. Four types of mechanically activated $MgCl_2$ samples are prepared using ball-milling in the absence and presence of different donors. The development of structural disorder along the grinding time is compared. It was found that the presence of donors accelerates the formation of δ-$MgCl_2$ in an early stage of grinding, while elongated grinding eventually results in δ-$MgCl_2$ with similar extents of structural disorder in the absence and presence of different donors. The FT-IR investigation consistently verified the morphological similarity between the firmly ground samples. Thus, the structure of δ-$MgCl_2$ is likely governed by mechanical energy when sufficiently ground.

Keywords: Ziegler–Natta catalysts; structural disorder; δ-$MgCl_2$; nanocrystal; morphology; synchrotron X-ray total scattering; atomic pair distribution function; FT-IR spectroscopy; mechanical activation; ball-milling

1. Introduction

$MgCl_2$-supported Ziegler–Natta catalysts (ZNCs) have played a central role in the production of stereoregular polypropylene for decades [1]. For preparing a performant ZNC, the $MgCl_2$ support has to be "activated". The activated support is generally termed as δ-$MgCl_2$ and featured with a broad powder X-ray diffraction (PXRD) pattern [2–4]. It has been considered that δ-$MgCl_2$ corresponds to nanosized crystallites (below ~30 nm) that are featured with rotational faults in the stacking of Cl–Mg–Cl layers [5–8]. However, such a consideration has solely relied on an interpretation of featureless PXRD patterns, and it has not been cross-validated with other analytical methods. For example, the solid-state NMR approach [9,10] has successfully distinguished bulk and nanosized $MgCl_2$, but the variation of the samples was limited, and the ability toward complementary analysis against PXRD is still to be improved. Recently, many computational studies treated $MgCl_2$ nanoparticle models instead of the infinite surfaces [11–13]; however, they are generally far smaller than the experimentally determined dimensions, and the structural characters other than the surfaces were hardly discussed. Therefore, the possibility of other structural disorders that can cause a similarly diffuse PXRD pattern, such as the

local atomic displacement from the ideal coordination places, lattice distortion, or another concept of amorphous-like structures [14], could not be excluded.

In recent publications [4,15], we revisited the identity of δ-$MgCl_2$ with the aid of cutting-edge analytical methods in terms of crystalline structure as well as surface morphology. In particular, the synchrotron X-ray total scattering technique was first applied to the structural investigation of δ-$MgCl_2$. The X-ray total scattering measurement enables us to access the ordered structure information (PXRD pattern) and the real space information via atomic pair distribution function (PDF). PDF directly shows local structure of atoms below sub-nanometers to medium or long distances of approximately 1 to 100 nm [16–19], which is exactly relevant for δ-$MgCl_2$. The PXRD pattern and the PDF were acquired through the X-ray total scattering measurement for a fourth-generation Ziegler–Natta catalyst. They were independently used to derive molecular models. Comparison between the two best-fit models revealed the structure of δ-$MgCl_2$ in a quantitative and cross-validated manner. It was concluded that the structure of δ-$MgCl_2$ is described by disorderly stacked $MgCl_2$ nanoplates. Moreover, vibrational spectroscopies and DFT calculations were applied on the same set of samples, and the obtained morphological insight into the activated δ-$MgCl_2$ was well consistent with the structural analysis results.

Here, we have adopted the same strategy to reveal the formation of δ-$MgCl_2$ and the involvement of donors therein: The structural evolution of $MgCl_2$ was quantitatively investigated during mechanical activation in the presence or absence of different donors by means of the synchrotron X-ray total scattering as well as vibrational spectroscopies. The structure of δ-$MgCl_2$ in the obtained samples was quantitatively determined with the aid of simulation using $MgCl_2$ nanoparticle models. The effect of donors was discussed on the formation of δ-$MgCl_2$. The mechanical activation is rather outdated and rarely applied in recent industry. However, it is suitable as the first step to clarify the formation of δ-$MgCl_2$ due to its chemical simplicity as well as to the ease of controlling the activation process through the grinding time. As the modern ZNCs possess a high performance as a consequence of the complex interaction among various components over atomic to macroparticle scale [20], the accumulation of fundamental knowledge is important for not only academia, but also industry. In such a sense, the effect of donors on the formation of δ-$MgCl_2$ is one of the issues that must be clarified. To the best of our knowledge, nobody has quantitatively determined the structure of mechanically activated δ-$MgCl_2$.

2. Results and Discussion

Mechanically activated δ-$MgCl_2$ samples were prepared by ball-milling with different grinding durations (3, 6, 12, 24, and 48 h) in a dry condition. To investigate the effect of donors on mechanical activation, the other two series of samples were prepared in the presence of typical donors ethylbenzoate (EB) and di-*n*-buthylphthalate (DBP). The amount of donors was set to the molar ratio of $MgCl_2$:donor = 16:1 mol/mol [20]. It is considered that donors play two distinct roles in mechanical activation [21]: (i) Capping effect by adsorbing on coordinatively unsaturated Mg^{2+} ions that are newly exposed in the course of grinding, and (ii) physical effects such as absorption of collision energy as a liquid and adhering particles by wetting their surfaces. Taking this speculation into account, using an inert liquid additive instead of donors would be worthwhile in terms of distinguishing the two roles. Toluene was chosen as the inert additive as it has no functional groups that can adsorb on Mg^{2+} ions while it contains an aromatic ring similar to EB and DBP. We thus prepared four series of samples (Dry-xx, EB-xx, DBP-xx, and Tol-xx; xx is the grinding duration in hours) to be subjected to synchrotron X-ray total scattering measurement. The derived high-quality PXRD patterns and PDF results allowed us to quantitatively compare the vertical and lateral dimensions as well as the stacking disorder of nanosized δ-$MgCl_2$ crystallites with the aid of simulation using $MgCl_2$ nanoparticle models. Moreover, the time-course development of δ-formation by mechanical activation was investigated.

The PXRD patterns of the mechanically activated $MgCl_2$ samples are summarized in Figure 1. The pristine $MgCl_2$ exhibited intense and sharp diffraction peaks, which can be assigned as α-$MgCl_2$

(Figure 1A). Diffraction peaks in all the other series of samples were weakened and broadened along with the grinding time regardless of the absence (B) or presence of additives (C, D, E). In particular, the intense two peaks that relates to the body-diagonal direction, (012) and (104), eventually merged into one broad peak at ~25–40° in 2θ in any series of samples. This indicates the occurrence of the stacking disorder among $MgCl_2$ crystalline layers [4]. Weakening of the (003) and (110) diffraction peaks corresponds to miniaturization of $MgCl_2$ crystallites in the *c*-direction (thinning) and the *a*,*b*-directions, respectively [4]. In comparison with the additive free samples (Figure 1B), the presence of EB and DBP evidently accelerated the conversion into δ-$MgCl_2$ (Figure 1C,D). The acceleration was more obvious for DBP. Note that DBP-3–24 remained pronounced sharp diffraction peaks that can be assigned as (012), (006), (104), and (110) of α-$MgCl_2$ over the diffuse pattern of δ-$MgCl_2$. This fact suggests a significant distribution in the crystallite structure. Such inhomogeneity was not observed for the other series of samples. Different consequences were obtained by the addition of toluene (Figure 1E): In Tol-6 and 12, all the diffraction peaks were sharper than those of Dry-6 and 12. This fact suggests that the addition of an inert liquid dissipates the mechanical energy to slow down both the crystallite miniaturization and stacking disorder. Nonetheless, further grinding led to similarly broad diffraction peaks compared to the dry samples (Tol-24,48 vs. Dry-24,48). As an example of chemically activated δ-$MgCl_2$, a ZNC sample that was prepared from $Mg(OEt)_2$ using DBP as a donor was also subjected to the analysis (Figure 1F) [4]. Note that its $MgCl_2$:DBP molar ratio of 15:1 is very close to 16:1 of the DBP-xx samples. It can be seen that the most finely grounded δ-$MgCl_2$ sample (DBP-48) still remains a more ordered structure compared to the $Mg(OEt)_2$-based catalyst. To quantify the progress of the δ-$MgCl_2$ conversion, the experimental PXRD patterns were fit with simulated patterns derived from $MgCl_2$ nanoparticle structure models [4]. A typical fitting result is shown in Figure S1. The determined structural parameters are summarized together with PDF fitting results and described later.

PDFs that were derived from the total scattering data are shown separately in long-range and short-range regions (Figure 2). The PDF of the $Mg(OEt)_2$-based catalyst is also given. A PDF includes a lot of important structural information. The peak positions directly correspond to atomic distances; specifically, the first peak at 0.25 nm reflects the closest Mg–Cl atomic pairs, and the second peak at 0.36 nm corresponds to the next closest atomic pairs (Cl–Cl and Mg–Mg pairs) [4]; therefore, the broadness of the peaks relates to the atomic displacement from the ideal positions. Besides, the intensity of the peaks reflects the relative abundance of the atomic pairs, and thus the damping of the peaks along with *r* is generally related to the finite crystalline dimensions. For δ-$MgCl_2$, the stacking disorder also causes intensity damping because it spoils the out of plane structural order [4]. In the long-range region (Figure 2A), almost no damping was observed for pristine $MgCl_2$ up to 10 nm, indicating that its crystallite dimension is sufficiently larger than 10 nm. For Dry-3, the peaks did not disappear at r = 10 nm, but the intensity around 10 nm was relatively smaller compared to the pristine $MgCl_2$. Judging from the sharpness of (003) and (110), the damping was most probably induced by the stacking disorder. On the basis of this speculation, the probability of α-$MgCl_2$ sequence (P_c, see Section 3.3) was determined by PDF fitting with $MgCl_2$ structure models in an infinite particle boundary mode. Note that it is not affordable by PXRD fitting due to the computationally infeasible size of the crystallite. P_c of EB-3 was also determined by the same method. On the other hand, Dry-6, Dry-12, Dry-24, Dry-48, EB-24, DBP-24, and Tol-24 exhibited significant decay, reflecting the fact that their crystallite dimensions are much smaller compared to the former described samples. The average crystallite dimension of those samples was also estimated by PDF fitting as *D* (Table S1, see Section 3.4 for details) and the results were well consistent with the crystallite dimension derived from the PXRD patterns. In the short-range region (Figure 2B), the peak positions and their broadness remained unchanged from those of pristine $MgCl_2$ for all the samples. This indicates that the local structure of $MgCl_2$ is not affected by mechanical or chemical activation as well as the presence of organic additives including donors. The results of PDF fitting also support this conclusion as the lattice constants ($l_{a,b,c}$) as fitting parameters were quite similar to each other (cf. Table 1). A typical fitting result and the obtained fitting parameters are shown in Figure S2 and Table S1.

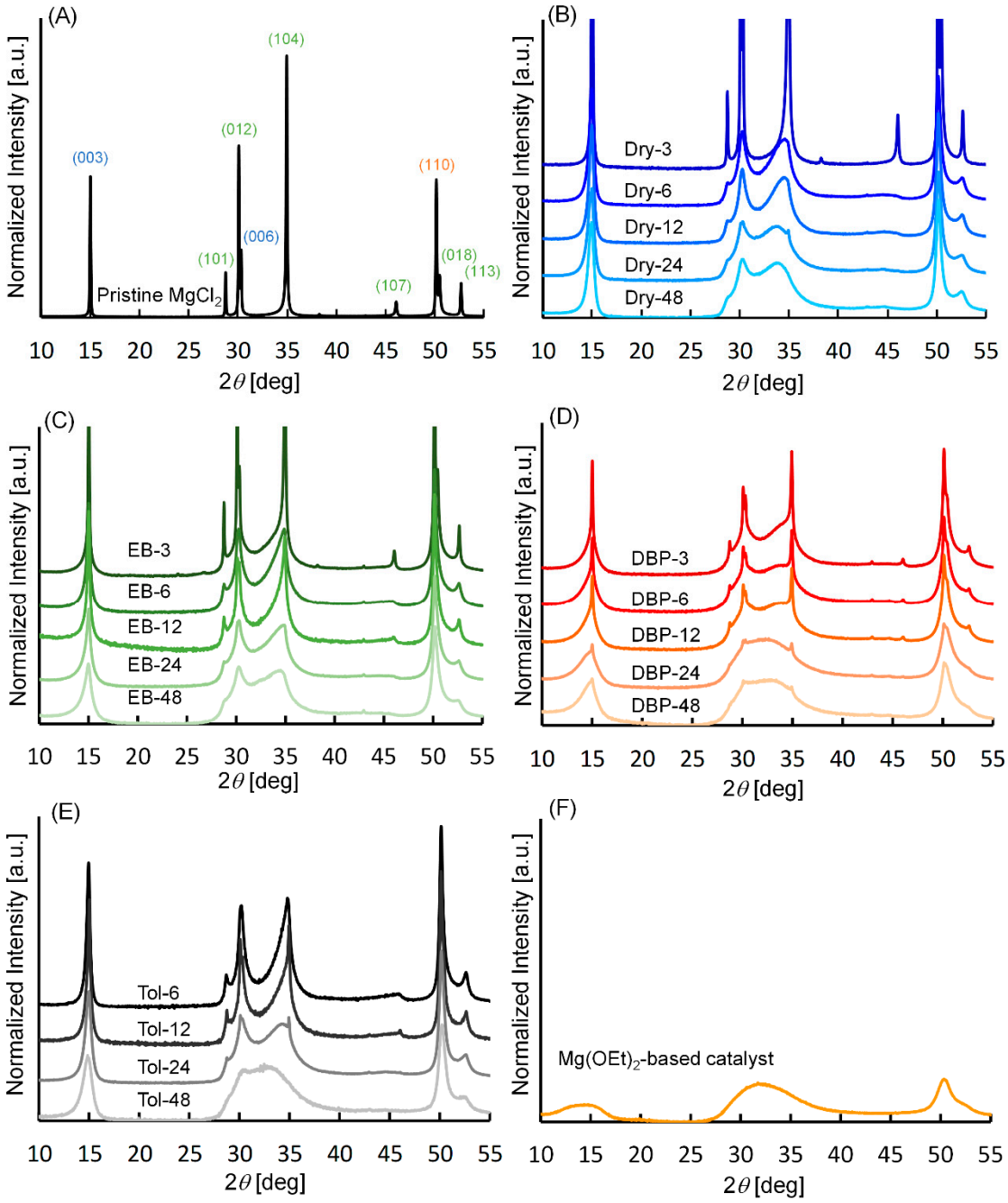

Figure 1. Powder X-ray diffraction (PXRD) patterns of mechanically activated $MgCl_2$ samples. (**A**) Pristine $MgCl_2$. (**B**) $MgCl_2$ samples ball-milled in a dry condition without adding organic additives. $MgCl_2$ samples ball-milled with (**C**) EB, (**D**) DBP, and (**E**) toluene. Dry-xx, EB-xx, DBP-xx, and Tol-xx, where xx is the grinding duration in hours. (**F**) $Mg(OEt)_2$-based catalyst as a typical example of chemically activated δ-$MgCl_2$. The same vertical scale is applied in panels (B–F), except in panel (A) due to the highly crystalline feature of pristine $MgCl_2$.

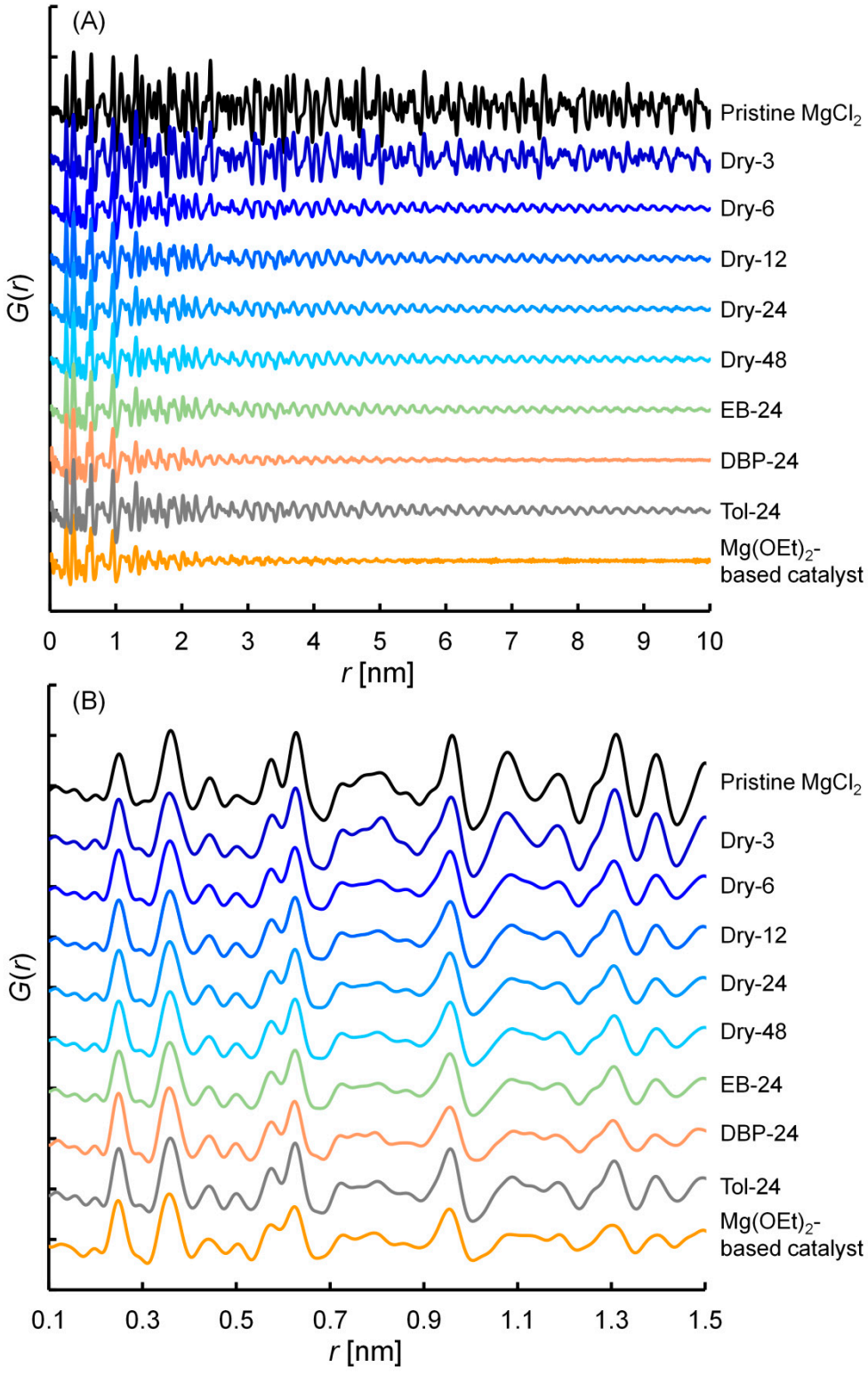

Figure 2. Atomic pair distribution functions (PDFs) of mechanically activated $MgCl_2$ samples. Long-range and short-range regions are separately represented in panels (**A**,**B**). The sample names exhibit the grinding condition, the type of additives and grinding duration in hours. $Mg(OEt)_2$-based catalyst is a typical example of chemically activated δ-$MgCl_2$.

The four structural parameters, P_c, L_c, and $L_{a,b}$ were determined via PXRD and PDF fitting. They are listed in Table 1, and its graphical summary is provided in Figure 3. As was discussed on the

basis of qualitative observation in Figures 1 and 2, the stacking disorder (Figure 3A) as well as the crystallite miniaturization (Figure 3B,C) promoted along with the grinding time. It was found that the crystallite miniaturization underwent in an isotropic manner: There was no significant difference between the values of L_c and $L_{a,b}$. This is somewhat interesting in a sense that the repetition along the *c*-axis is based on the weak van der Waals interaction with respect to the ionic bonding along the *a*,*b*-axes. The mechanical force which was isotropically imposed with a sufficient energy to break the ionic bonds plausibly explains the result. Note that δ-$MgCl_2$ possessed a platelet crystallite morphology when chemically activated. Compared to the dry milled samples, the addition of toluene obviously decelerated the conversion into δ-$MgCl_2$. Specifically, P_c, L_c, and $L_{a,b}$ of Dry-6–12 were 58–55%, 13–13 nm, and 13–13 nm, respectively, while those of Tol-6–12 were 82–64%, 29–16 nm, and 29–16 nm, respectively. This could be explained by the physical effects that the presence of a liquid absorbed the collision energy. However, the extent of disorder eventually reached a similar level to that of the dry milled sample at the longest grinding time (P_c, L_c, $L_{a,b}$: 40%, 12 nm, and 11 nm for Dry-48, respectively, while 31%, 8 nm, and 9 nm for Tol-48, respectively). Contrary, the addition of donors accelerated the δ-$MgCl_2$ formation as is shown in the reduction of the three structural parameters at 3 h: P_c, $L_{a,b}$, L_c: 91%, 57 nm, 54 nm for Dry-3; 88%, 39 nm, 42 nm for EB-3; and 55%, 13 nm, 13 nm for DBP-3, respectively. In particular, DBP most effectively accelerated the δ-$MgCl_2$ formation. It is clear that the stabilization of lateral surfaces through chemisorption accelerates the miniaturization along the *a*,*b*-axes. On the other hand, the mechanical grinding generally leads to isotropic particles [22,23]. It is considered that the miniaturization along the *a*,*b*-axes increases a chance of collision at lateral surfaces and thus in turn promotes the miniaturization along the *c*-axis. The promoting effect of the adsorption overcomes the retarding role of a liquid additive.

As stated above, the addition of additives exerted significant influences on the progress of the δ-formation. On the other hand, when samples were compared at the longest grinding duration (48 h), only small structural differences were found. More in details, according to the data reported in Table 1 and visualized in Figure 3, both donors slightly promote nanosizing and disorder, DBP a little bit more, while EB at the same level as toluene. Anyhow, it is generally known that the size of particles that can be reached by ball-milling largely depends on other grinding conditions, in particular the size of the balls [24], which plausibly explains the small differences. Finally, the structure of DBP-48 is compared with that of the chemically activated sample in the presence of DBP ($Mg(OEt)_2$-based catalyst). The P_c and the lateral dimensions, $L_{a,b}$ were similar (31% and 9 × 4 nm vs. 25% and 8 × 3 nm), while there was a large difference in the *c*-axis dimension (6 nm vs. 1 nm). This fact suggests that the structure of δ-$MgCl_2$ largely depends on the preparation protocol.

Table 1. PXRD fitting results for mechanically activated $MgCl_2$ samples.

Sample Name	P_c [%]	$L_a \times L_b$ [nm]	L_c [nm]
Pristine $MgCl_2$	100 [1]	61.5 [2]	72.4 [2]
Dry-3	91 [3]	56.8 [1]	54.2 [1]
Dry-6	58	12.7 × 12.7	13.3
Dry-12	55	12.7 × 12.7	13.3
Dry-24	40	10.9 × 10.9	11.5
Dry-48	40	10.9 × 10.9	11.5
EB-3	88 [3]	38.7 [2]	41.5 [2]
EB-6	58	14.5 × 14.5	13.3
EB-12	58	14.5 × 14.5	13.3
EB-24	55	10.9 × 10.9	10.3
EB-48	46	9.1 × 9.1	8.0
DBP-3	55	12.7 × 12.7	13.3
DBP-6	34	9.1 × 9.1	9.7
DBP-12	37	10.9 × 10.9	8.0
DBP-24	31	9.1 × 3.6	6.2
DBP-48	31	9.1 × 3.6	6.2

Table 1. *Cont.*

Sample Name	P_c [%]	$L_a \times L_b$ [nm]	L_c [nm]
Tol-6	82	29.1 × 29.1	29.2
Tol-12	64	16.4 × 16.4	16.2
Tol-24	46	12.7 × 12.7	11.5
Tol-48	31	9.1 × 9.1	8.0
$Mg(OEt)_2$-based catalyst	25	7.6 × 3.3	0.9

[1] Pristine $MgCl_2$ was confirmed as highly crystalline α-$MgCl_2$ from the PXRD pattern (Figure 1A). Thus, 100% of P_c was assumed. [2] The crystallite dimensions are too large to simulate the PXRD pattern based on the Debye equation. Instead, the Scherrer equation and the full-width at half-maximum (FWHM) of the (003) and (110) diffraction peaks were used to calculate the crystallite dimensions [25]. ($D_{hkl} = 0.94\lambda\beta^{-1}\cos\theta^{-1}$, λ: X-ray wavelength, β: FWHM of the diffraction peak, θ: diffraction angle of the peak). [3] P_c was determined by PDF fitting using $MgCl_2$ structure models in an infinite particle boundary mode. The structure which led to the lowest $R_{w,PDF}$ value was considered as the best-fit model.

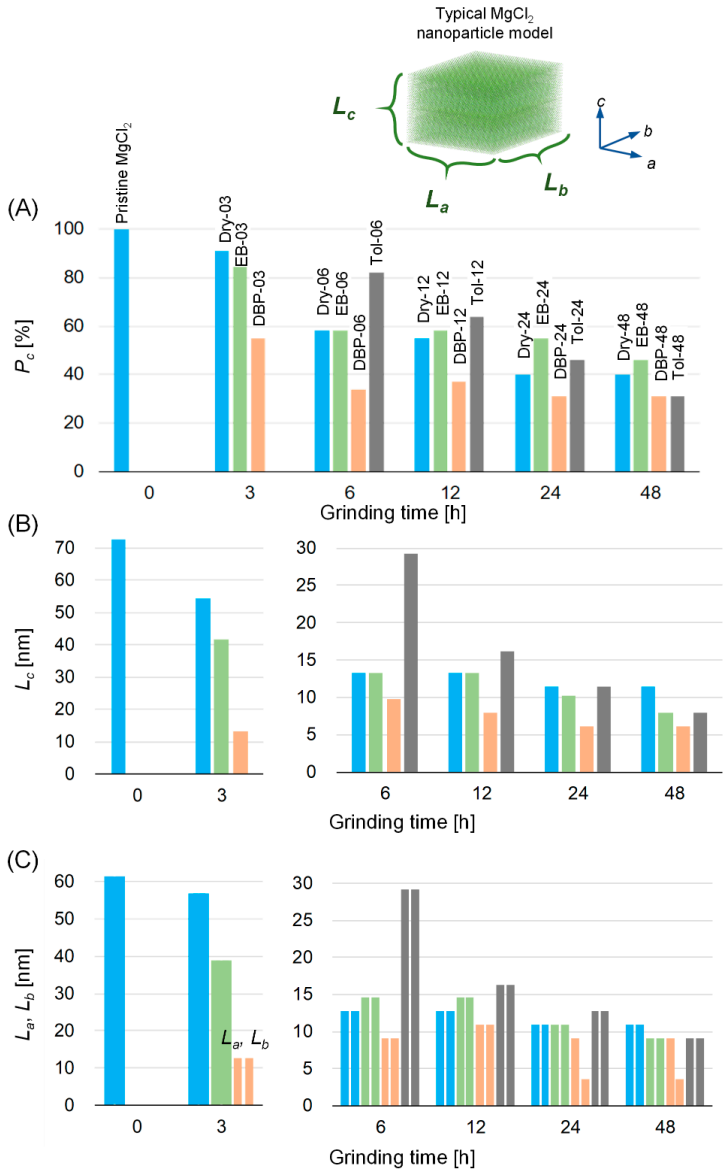

Figure 3. Development of structural disorder along with the grinding time. $MgCl_2$ samples ball-milled in a dry condition (blue). $MgCl_2$ samples ball-milled in the presence of EB (green), DBP (orange), or toluene (gray). Four structural parameters, (**A**) P_c, (**B**) L_c, and (**C**) L_a and L_b, were determined by PXRD fitting or PDF fitting (Table 1). A typical δ-$MgCl_2$ nanoparticle model is shown in the above.

Finally, FT-IR spectroscopy (in both mid and far IR regions) was performed on the samples at the longest grinding time, in order to assess the possibly different effects of the different mechanical treatments on $MgCl_2$ morphology. In particular, the investigation focused on the comparison between the dry ball-milling and the ball-milling in the presence of the electron donors (in Figure 4), in order to verify their role as capping agents.

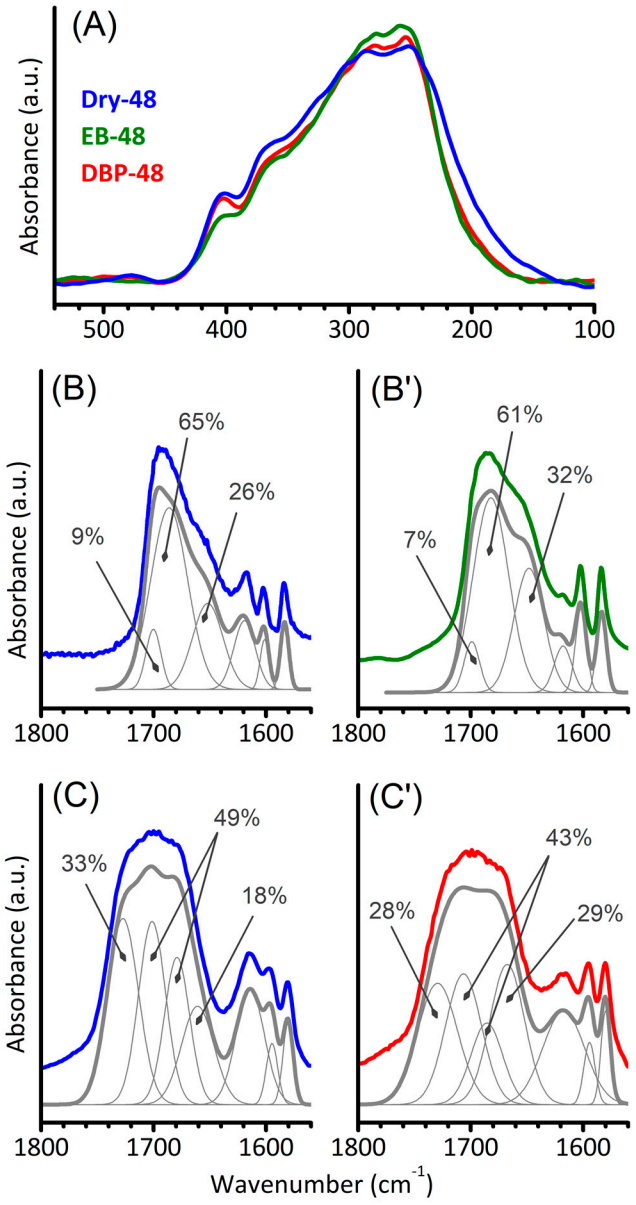

Figure 4. (**A**) Far IR spectra of Dry-48, EB-48 and DBP-48 samples. (**B**,**B'**) Curve fitting of FT-IR spectra in the ν(C=O) region for EB adsorbed on Dry-48 and for EB-48, respectively. (**C**,**C'**) The same as B and B' for DBP adsorbed on Dry-48 and for DBP-48, respectively. Percentages are reported for the signals associated to the donors' carbonyls, according to literature.

Figure 4A displays the Far IR spectra of the three samples. Such spectra are dominated by a broad absorption centered at 250 cm^{-1}, which is due to Mg–Cl vibrations and we have recently demonstrated to be sensitive to the relative extent of $MgCl_2$ surfaces [15]. In particular, the spectrum of Dry-48 is the spectrum with a larger absorption at low wavenumbers (~220 cm^{-1}), where the bulk and the basal (001) surface mostly contribute. The spectra of EB-48 and DBP-48 are very similar to each other, slightly differing only at high wavenumbers, indicating a slight difference in the relative extent of the lateral

surfaces that give absorption in that region; in particular the spectrum of DBP-48 displays a more pronounced band at 405 cm^{-1}, indicating that DBP more effectively stabilizes the surfaces presenting an absorption there around, i.e., (110), (012), and (015) according to DFT simulations [15].

Afterwards, in order to get a deeper insight on the surface properties of δ-$MgCl_2$, the IR fingerprints of the donors were analyzed as internal molecular probes, comparing those results with the IR fingerprints of the same donors adsorbed on Dry-48 sample (and outgassed at 90 °C under dynamic vacuum to remove the excess). A curve fitting analysis was applied to the signals in the 1800–1550 cm^{-1} region, identifying each contribution on the base of the literature.

For what concerns EB (Figure 4(B,B′)), the signals were interpreted as ν(C=O) of EB in interaction with 5-coordinated Mg^{2+} (on (104) surface) at 1700 cm^{-1}, with 4-coordinated Mg^{2+} (on (110), (012), and (015) surfaces) at 1680 cm$-^{1}$, and with 3-coordinated Mg^{2+} (defects) at 1650 cm^{-1}, alongside the δ(OH) of a few traces of adventitious water contaminations at 1620 cm^{-1} and two vibrational modes of the phenyl ring at 1602 and 1583 cm^{-1} [26,27]. Although a quantitative analysis should have required the extinction coefficients, the relative proportion of the ν(C=O) bands (reported as percentage in Figure 4) reveals that in EB-48 sample there are a little bit more defects than in Dry-48 (32 to 26%) and that the ratio between 4 and 5-coordinated Mg^{2+} sites is slightly higher in EB-48 than in Dry-48 (61:7 with respect to 65:9).

Analogously, also the spectrum of DBP (Figure 4(C,C′)) presents two vibrational modes of the phenyl ring (at 1580 and 1595 cm^{-1}), the δ(OH) of a few water traces and several bands assigned to the ν(C=O) of different DBP molecules. In particular, the band at 1730 cm^{-1} is due to liquid-like physisorbed DBP, the bands at 1705 and 1680 cm^{-1} are overall due to DBP on surfaces, and the band at 1660 cm^{-1} is due to DBP on defects [26,28,29]. In agreement with what observed upon EB analysis, DBP-48 presents more defects than Dry-48 (29 to 18%), whereas in Dry-48 there is a higher amount of liquid-like DBP (33 to 28%), likely because when DBP is adsorbed in a second step the aspecific physisorption is favored. Unfortunately, DBP does not allow distinguishing among $MgCl_2$ surfaces, since ν(C=O) for DBP on surface Mg^{2+} sites depends not only on Mg^{2+} acidic strength but also on DBP configuration (e.g., monodentate or chelate) [29].

Overall, the FT-IR morphological investigation pointed out that ball-milling in the presence of donors favors the expression of lateral surfaces rather than the basal one and the presence of defects, in well agreement with recent theoretical studies [30–32]. However, the differences with Dry-48 sample are really small (as observed in the structural analysis), reasonably because other grinding parameters play a more important role, such as the size of the balls [24].

3. Materials and Methods

3.1. Sample Preparation

All the samples were prepared by mechanically grinding a highly crystalline $MgCl_2$ powder, which was donated by Toho Titanium Co., Ltd. (Kanagawa, Japan). A 0.5 L stainless-steel pot was charged with 25 g of pristine $MgCl_2$ and 235 stainless-steel balls (10 mm diameter) under an inert atmosphere. Then, the mixture was ground for 3, 6, 12, 24, or 48 h on a planetary ball mill (Sansho Industry Co., Ltd., Osaka, Japan, a custom-made model). Grinding was performed (i) in a dry condition, and in the presence of (ii) 2.3 mL of ethylbenzoate (EB), (iii) 4.3 mL of di-*n*-buthylphthalate (DBP), or (iv) 2.3 mL of toluene (Tol). These chemicals were purchased from FUJIFILM Wako Pure Chemical Corporation (Tokyo, Japan) and dried over 4A molecular sieves prior to use. Thus prepared samples are termed as Dry, EB, DBP, Tol-xx: xx is the duration of the grinding in hours. All the samples were handled and stored under an inert atmosphere in order to minimize the moisture contamination.

3.2. X-ray Total Scattering Measurement

The details of the experiment were described in the previous literature [4]. Each powder sample was filled in a Lindemann glass capillary tube (0.3 mm internal diameter). The tube was flame-sealed

and subjected to X-ray total scattering experiment at beamline BL05S2 in Aichi Synchrotron Radiation Center (Aichi, Japan). The wavelength of X-ray was set to 0.69 Å (18.0 keV), and the scattered X-ray was collected by four 2D detectors in transmission geometry in the 2θ range of 3–132°. The scattering intensity for an empty capillary tube was subtracted as the background. In order for direct comparison with literature, the diffraction angle of the PXRD patterns was scaled to the wavelength of Cu Kα radiation (λ = 1.5418 Å).

3.3. PXRD Fitting

The acquired PXRD patterns were analyzed based on the comparison with the simulated patterns derived from $MgCl_2$ nanoparticle models by using DISCUS [33]. The basic concept was already reported in the previous literature [4]. Briefly, nanoparticle models were created based on four parameters: L_a, L_b, L_c, and P_c. The dimension in the lateral directions ($L_{a,b}$) is in accordance with unit cells repeated in the *a*,*b*-directions. The basal dimension (L_c) corresponds to the number of Cl-Mg-Cl layers stacked along the *c*-direction. The probability of α-$MgCl_2$ (ABCA) sequence (P_c) is tuned in 25–100% to express the stacking disorder. The rest 75–0% were equally distributed to β-$MgCl_2$ (ABAB) and the two rotational error sequences (ABAC, ABCB). The lattice constants were fixed as 0.3636 nm (l_a,l_b) and 0.5889 nm (l_c), which corresponds to the separation of neighboring Cl-Mg-Cl layers. The thickness of a single Cl-Mg-Cl layer was set to 0.2667 nm. These values were taken from experimentally determined lattice constants of α-$MgCl_2$ [34]. An adequate number of models were generated for a single set of parameters, and their PXRD or PDFs were averaged in order to express stacking probability. The presence of organic additives was disregarded because they composed of only light atoms (H, C, and O) having the very low X-ray scattering power.

Debye scattering equation was used to simulate the PXRD pattern from a $MgCl_2$ structure model with the aid of DISCUS [33],

$$I_{calc}(Q) = \sum_i \sum_j f_i f_j \frac{\sin\left(2\pi Q r_{ij}\right)}{2\pi Q r_{ij}}, \tag{1}$$

where $I(Q)$ is the scattering intensity at scattering vector Q ($4\pi\sin\theta/\lambda$), f_i, f_j, and r_{ij} are, respectively, the X-ray atomic scattering factors for *i*th and *j*th atoms, and the distance between the two atoms. This equation inherently depicts the orientation-averaged scattering intensity from a particle model and includes the finite crystallite size effect (peak broadening) [35]. The difference between a simulated and an experimental pattern (($I_{\mathrm{calc}}(2\theta)$) and $I_{\mathrm{exp}}(2\theta)$) was derived by

$$R_{w,PXRD} = \left[\frac{\sum\left(I_{exp}(2\theta) - I_{calc}(2\theta)\right)^2}{\sum I_{exp}(2\theta)^2}\right]^{\frac{1}{2}}. \tag{2}$$

The four structural parameters were recursively modified to minimize the difference, $R_{w,\mathrm{PXRD}}$.

3.4. Acquisition and Fitting of PDF

A reduced atomic pair distribution function ($G_{\mathrm{exp}}(r)$) was converted from the total scattering data using software PDFgetX2 [36]. To acquire the total scattering structure function, $S(Q)$, the 1D scattering data were corrected for X-ray polarization, Compton scattering, and atomic scattering factors. $G_{\mathrm{exp}}(r)$ is obtained by a Fourier transform of $S(Q)$ [17],

$$\begin{aligned} G_{exp}(r) &= \left(\tfrac{\pi}{2}\right) \int_{Q_{min}}^{Q_{max}} [S(Q) - 1] \sin(Qr) \mathrm{d}Q \\ &= 4\pi r[\rho(r) - \rho_0] \end{aligned}, \tag{3}$$

where Q, $\rho(r)$, and ρ_0 are the scattering vector, the atomic pair density distribution, and the average atomic density, respectively. The Q range for the Fourier transform was set as 0.55 to 15 0.55 Å^{-1} as Q_{max} and Q_{min}.

As with the PXRD fitting, the $G_{exp}(r)$ was compared with simulated $G_{calc}(r)$ with software PDFgui [37]. $G_{calc}(r)$ was calculated with a given nanoparticle model by using the following equations,

$$G_{calc}(r) = \left(G'_{calc} * S\right)(r), \tag{4}$$

$$G'_{calc}(r) = B(r)\left(\frac{1}{Nr}\sum_i\sum_j\left[\frac{c_i c_j f_i f_j}{f^2}T_{ij}(r)\right] - 4\pi r\rho_0\right), \tag{5}$$

$$T_{ij}(r) = \frac{1}{\sqrt{2\pi}\sigma_{ij}}exp\left[-\frac{\left(r-r_{ij}\right)^2}{2\sigma_{ij}^2}\right], \tag{6}$$

$$S(r) = \frac{sin(Q_{max}r)}{r}, \tag{7}$$

where N is the number of atoms and c_i is the relative abundance of the ith element. σ_{ij} is the broadening factor including anisotropic displacement parameters as well as correlation motion of the atoms. These parameters were recursibly updated to reduce the residual $R_{w,PDF}$,

$$R_{w,PDF} = \left[\frac{\sum\left(G_{exp}(r_i) - G_{calc}(r_i)\right)^2}{\sum G_{exp}(r_i)^2}\right]^{\frac{1}{2}}, \tag{8}$$

$B(r)$ is a damping factor regarding the resolution of instruments. Q_{damp} was acquired with a standard sample and set as constant. The broadening derived from the limited Q_{max} value was incorporated by $S(r)$. The finite object effect was taken into account by applying a spherical shape function of Equation (9),

$$\gamma_{Sphere}(r,\ D) = \begin{cases} 1 - \frac{3}{2}\left(\frac{r}{D}\right) + \frac{1}{2}\left(\frac{r}{D}\right)^3 & (r \le D) \\ 0 & (r > D) \end{cases}, \tag{9}$$

where D expresses the diameter of the spherical object, which is a built-in function of PDFgui. The effectiveness of this approximation was already confirmed for mechanically activated samples [4].

3.5. Acquisition of FT-IR Spectra

FT-IR spectra were acquired in transmission mode with a Bruker Vertex70 instrument, both in the Mid-IR (with an MCT detector) and in the Far-IR (with a DTGS detector). In both cases, the samples were prepared in glove-box as thin layers on a Si wafer (using hexane as a suspending agent), and placed inside a quartz measurement cell connected to a vacuum line to control the atmosphere on the samples during the FT-IR acquisition; the cell was equipped with two KBr windows for Mid-IR spectra, or with two polyethylene windows for Far-IR ones. All the acquired spectra are shown in absorbance, after subtracting the weak contributions of the Si wafer and of the cell windows.

4. Conclusions

In the current study, we attempted to investigate the formation of δ-$MgCl_2$ by mechanical activation with or without donors. The δ-$MgCl_2$ samples were prepared with planetary ball-milling in various grinding durations in the absence or presence of donors (ethylbenzoate (EB), di-*n*-buthylphthalate (DBP), or toluene as a non-coordinative liquid additive). Quantitative structural determination by synchrotron X-ray total scattering revealed that the activation was accelerated by the addition of donors, which was probably caused by stabilization of lateral surfaces of crystallites through chemisorption.

However, the structure and morphology of δ-$MgCl_2$ reachable at a sufficiently long grinding duration were only slightly affected by the additives, in terms of promotion of nano-sizing, disorder and defects. It was concluded that donors accelerate the δ-$MgCl_2$ formation, but its influence cannot overcome the impact of the activation protocol or conditions.

Supplementary Materials: The following are available online at http://www.mdpi.com/2073-4344/10/9/1089/s1, Figure S1: Typical PXRD fitting result, Figure S2: Typical PDF fitting result, Table S1: Results of PDF fitting with PDFgui.

Author Contributions: Conceptualization, T.T.; methodology, T.W. and A.P.; investigation, T.W., A.P., and A.T.; data curation, T.W. and A.P.; writing—original draft preparation, T.W. and A.P.; writing—review and editing, A.T., P.C., M.T., E.G., and T.T.; visualization, T.W., A.P. and P.C.; supervision, E.G. and T.T.; project administration, T.T.; funding acquisition, P.C., M.T., E.G., and T.T. All authors have read and agreed to the published version of the manuscript.

Funding: The work of T.W., A.P., C.P., M.T., E.G., and T.T. forms part of the research programme of DPI, project #802.

Acknowledgments: The X-ray total scattering experiments were conducted at the BL5S2 of Aichi Synchrotron Radiation Center, Aichi Science & Technology Foundation, Aichi, Japan (proposal numbers: 201803029).

Conflicts of Interest: The authors declare no conflict of interest. The funder had no role in the design of the study; in the collection, analyses, or interpretation of data; in the writing of the manuscript; or in the decision to publish the results.

References

1. Busico, V. Giulio Natta and the development of stereoselective propene polymerization. In *Polyolefins: 50 Years after Ziegler and Natta I Polyolefins: 50 Years after Ziegler and Natta I Polyethylene and Polypropylene*; Advances in Polymer Science 257; Kaminsky, W., Ed.; Springer-Verlag: Berlin/Heidelberg, Germany, 2013; pp. 37–57.
2. Bassi, I.W.; Polato, F.; Calcaterra, M.; Bart, J.C.J. A new layer structure of $MgCl_2$ with hexagonal close packing of the chlorine atoms. *Z. Krist. New Cryst. Struct.* **1982**, *159*, 297–302. [CrossRef]
3. Di Noto, V.; Bresadola, S. New synthesis of a highly active δ-$MgCl_2$ for $MgCl_2/TiCl_4/AlEt_3$ catalytic systems. *Macromol. Chem. Phys.* **1996**, *197*, 3827–3835. [CrossRef]
4. Wada, T.; Takasao, G.; Piovano, A.; D'Amore, M.; Thakur, A.; Chammingkwan, P.; Bruzzese, P.C.; Terano, M.; Civalleri, B.; Bordiga, S.; et al. Revisiting the identity of δ-$MgCl_2$: Part I. Structural disorder studied by synchrotron X-ray total scattering. *J. Catal.* **2020**, *385*, 76–86. [CrossRef]
5. Zannetti, R.; Marega, C.; Marigo, A.; Martorana, A. Layer-lattices in Ziegler-Natta catalysts. *J. Polym. Sci. Part. B Polym. Phys.* **1988**, *26*, 2399–2412. [CrossRef]
6. Busico, V.; Causà, M.; Cipullo, R.; Credendino, R.; Cutillo, F.; Friederichs, N.; Lamanna, R.; Segre, A.; Van Axel Castelli, V. Periodic DFT and high-resolution magic-angle-spinning (HR-MAS) ^1H NMR investigation of the active surfaces of $MgCl_2$-supported Ziegler-Natta catalysts. The $MgCl_2$ matrix. *J. Phys. Chem. C* **2008**, *112*, 1081–1089. [CrossRef]
7. Marigo, A.; Marega, C.; Zannetti, R.; Morini, G.; Ferrara, G. Small- and wide-angle X-ray scattering analysis of Ziegler-Natta catalysts: Structural disorder, surface area and activity. *Eur. Polym. J.* **2000**, *36*, 1921–1926. [CrossRef]
8. Takasao, G.; Wada, T.; Thakur, A.; Chammingkwan, P.; Terano, M.; Taniike, T. Machine learning-aided structure determination for $TiCl_4$–capped $MgCl_2$ nanoplate of heterogeneous Ziegler-Natta catalyst. *ACS Catal.* **2019**, *9*, 2599–2609. [CrossRef]
9. Blaakmeer, E.S.M.; Antinucci, G.; Busico, V.; van Eck, E.R.H.; Kentgens, A.P.M. Solid-state NMR investigations of $MgCl_2$ catalyst support. *J. Phys. Chem. C* **2016**, *120*, 6063–6074. [CrossRef]
10. Blaakmeer, E.S.M.; Antinucci, G.; Correa, A.; Busico, V.; van Eck, E.R.H.; Kentgens, A.P.M. Structural characterization of electron donors in Ziegler-Natta catalysts. *J. Phys. Chem. C* **2018**, *122*, 5525–5536. [CrossRef]
11. Zorve, P.; Linnolahti, M. Saturation of magnesium dichloride crystallites by titanium tetrachloride. *Surf. Sci.* **2020**, *699*, 121627. [CrossRef]

12. Breuza, E.; Antinucci, G.; Budzelaar, P.H.M.; Busico, V.; Correa, A.; Ehm, C. $MgCl_2$-supported Ziegler-Natta catalysts: A DFT-D "flexible-cluster" approach to internal donor adducts. *J. Phys. Chem. C* **2018**, *122*, 9046–9053. [CrossRef]
13. Credendino, R.; Pater, J.T.M.; Correa, A.; Morini, G.; Cavallo, L. Thermodynamics of formation of uncovered and dimethyl ether-covered $MgCl_2$ crystallites. consequences in the structure of Ziegler-Natta heterogeneous catalysts. *J. Phys. Chem. C* **2011**, *115*, 13322–13328. [CrossRef]
14. Suarez, S.; Di Noto, V.; Stallworth, P.E.; Abbrent, S.; Vittadello, M.; Alamgir, F.M.; Greenbaum, S.G.; Drain, C.M. Polymeric δ-$MgCl_2$ nanoribbons. *Inorg. Chim. Acta* **2006**, *359*, 2513–2518.
15. Piovano, A.; D'Amore, M.; Wada, T.; Bruzzese, P.C.; Takasao, G.; Thakur, A.; Chammingkwan, P.; Terano, M.; Civalleri, B.; Bordiga, S.; et al. Revisiting the identity of δ-$MgCl_2$: Part II. Morphology and exposed surfaces studied by vibrational spectroscopies and DFT calculation. *J. Catal.* **2020**, *387*, 1–11. [CrossRef]
16. Billinge, S.J.L. Nanoscale structural order from the atomic pair distribution function (PDF): There's plenty of room in the middle. *J. Solid State Chem.* **2008**, *181*, 1695–1700. [CrossRef]
17. Egami, T.; Billinge, S.J.L. (Eds.) *Underneath the Bragg Peaks*, 2nd ed.; Elsevier: Oxford, UK, 2012.
18. Bae, S.; Jee, H.; Suh, H.; Kanematsu, M.; Shiro, A.; Machida, A.; Watanuki, T.; Shobu, T.; Morooka, S.; Geng, G.; et al. Analysis of atomistic structural deformation characteristics of calcium silicate hydrate in 53-year-old tricalcium silicate paste using atomic pair distribution function. *Constr. Build. Mater.* **2020**, *237*, 117714. [CrossRef]
19. Christiansen, T.L.; Cooper, S.R.; Jensen, K.M.Ø. There's no place like real-space: Elucidating size-dependent atomic structure of nanomaterials using pair distribution function analysis. *Nanoscale Adv.* **2020**, *2*, 2234–2254. [CrossRef]
20. Taniike, T.; Funako, T.; Terano, M. Multilateral characterization for industrial Ziegler-Natta catalysts toward elucidation of structure–performance relationship. *J. Catal.* **2014**, *311*, 33–40. [CrossRef]
21. Taniike, T.; Terano, M. The use of donors to increase the isotacticity of polypropylene. In *Polyolefins: 50 Years after Ziegler and Natta I Polyolefins: 50 Years after Ziegler and Natta I Polyethylene and Polypropylene*; Advances in Polymer Science 257; Kaminsky, W., Ed.; Springer-Verlag: Berlin/Heidelberg, Germany, 2013; pp. 81–97.
22. Dutta, H.; Sahu, P.; Pradhan, S.K.; De, M. Microstructure characterization of polymorphic transformed ball-milled anatase TiO_2 by Rietveld method. *Mater. Chem. Phys.* **2003**, *77*, 153–164. [CrossRef]
23. Cui, B.Z.; Gabay, A.M.; Li, W.F.; Marinescu, M.; Liu, J.F.; Hadjipanayis, G.C. Anisotropic $SmCo_5$ nanoflakes by surfactant-assisted high energy ball milling. *J. Appl. Phys.* **2010**, *107*, 105–108. [CrossRef]
24. Shin, H.; Lee, S.; Suk Jung, H.; Kim, J.B. Effect of ball size and powder loading on the milling efficiency of a laboratory-scale wet ball mill. *Ceram. Int.* **2013**, *39*, 8963–8968. [CrossRef]
25. Chammingkwan, P.; Thang, V.Q.; Terano, M.; Taniike, T. MgO/$MgCl_2$/$TiCl_4$ Core–shell catalyst for establishing structure–performance relationship in Ziegler-Natta olefin polymerization. *Top. Catal.* **2014**, *57*, 911–917. [CrossRef]
26. Potapov, A.G.; Bukatov, G.D.; Zakharov, V.A. Drift study of internal donors in supported Ziegler-Natta catalysts. *J. Mol. Catal. A Chem.* **2006**, *246*, 248–254. [CrossRef]
27. Piovano, A.; D'Amore, M.; Thushara, K.S.; Groppo, E. Spectroscopic evidences for $TiCl_4$/Donor complexes on the surface of $MgCl_2$-supported Ziegler-Natta catalysts. *J. Phys. Chem. C* **2018**, *122*, 5615–5626. [CrossRef]
28. Cheruvathur, A.V.; Langner, E.H.G.; Niemantsverdriet, J.W.H.; Thüne, P.C. In situ ATR-FTIR studies on $MgCl_2$-diisobutyl phthalate interactions in thin film Ziegler-Natta catalysts. *Langmuir* **2012**, *28*, 2643–2651. [CrossRef]
29. Singh, G.; Kaur, S.; Makwana, U.; Patankar, R.B.; Gupta, V.K. Influence of internal donors on the performance and structure of $MgCl_2$ supported titanium catalysts for propylene polymerization. *Macromol. Chem. Phys.* **2009**, *210*, 69–76. [CrossRef]
30. Kuklin, M.S.; Bazhenov, A.S.; Denifl, P.; Leinonen, T.; Linnolahti, M.; Pakkanen, T.A. Stabilization of magnesium dichloride surface defects by mono- and bidentate donors. *Surf. Sci.* **2015**, *635*. [CrossRef]
31. Vanka, K.; Singh, G.; Iyer, D.; Gupta, V.K. DFT study of Lewis base interactions with the $MgCl_2$ surface in the Ziegler-Natta catalytic system: Expanding the role of the donors. *J. Phys. Chem. C* **2010**, *114*, 15771–15781. [CrossRef]
32. Shetty, S. Synergistic, reconstruction and bonding effects during the adsorption of internal electron donors and $TiCl_4$ on $MgCl_2$ surface: A periodic-DFT investigation. *Surf. Sci.* **2016**, *653*, 55–65. [CrossRef]

33. Proffen, T.; Neder, R.B. DISCUS, a program for diffuse scattering and defect structure simulations—Update. *J. Appl. Cryst.* **1999**, *32*, 838–839. [CrossRef]
34. Partin, D.E.; O'Keeffe, M. The structures and crystal chemistry of magnesium chloride and cadmium chloride. *J. Solid State Chem.* **1991**, *95*, 176–183. [CrossRef]
35. Scardi, P.; Billinge, S.J.L.; Neder, R.; Cervellino, A. Celebrating 100 years of the Debye scattering equation. *Acta Cryst. Sect. A Found. Adv.* **2016**, *72*, 589–590. [CrossRef] [PubMed]
36. Qiu, X.; Thompson, J.W.; Billinge, S.J.L. PDFgetX2: A GUI-driven program to obtain the pair distribution function from X-ray powder diffraction data. *J. Appl. Cryst.* **2004**, *37*, 678. [CrossRef]
37. Božin, E.S.; Billinge, S.J.L.; Proffen, T.; Farrow, C.L.; Juhas, P.; Bryndin, D.; Liu, J.W.; Bloch, J. PDFfit2 and PDFgui: Computer programs for studying nanostructure in crystals. *J. Phys. Condens. Matter* **2007**, *19*, 335219.